PERGAMON

International Journal of Heat and Mass Transfer 45 (2002) 3741–3757

International Journal of HEAT and MASS TRANSFER

www.elsevier.com/locate/ijhmt

Heat transfer enhancement in a grooved channel with curved vanes

Cila Herman *, Eric Kang

Department of Mechanical Engineering, The Johns Hopkins University, 3400 North Charles Street, Baltimore, MD 21218, USA

Received 10 October 2001; received in revised form 16 February 2002

Abstract

We visualize unsteady temperature fields in the grooved channel with curved vanes using holographic interferometry. The heat transfer performance of the investigated channel is compared with that of the basic grooved channel. The addition of curved vanes above the downstream end of the heated block redirects the flow from the main channel into the groove. Heat transfer shows an increase by a factor of 1.5–3.5, when compared to the basic grooved channel, mainly due to increased flow velocities in the groove region. Flow transition from steady to oscillatory occurs around $Re = 450$ and flow oscillations contribute to heat transfer enhancement. The pressure drop is 3–5 times higher than in the basic grooved channel.

1. Introduction

A great deal of research has been done to understand the subject of fluid flow and heat transfer in grooved channels and related geometries, such as backward facing steps, channel expansions and cavities. Grooved channels are frequently encountered in a whole range of practical applications, including heat transfer surfaces of heat exchangers, cooling of electronic equipment and nuclear reactor cores, as well as biomedical and aerospace applications. However, numerous questions, especially those regarding unsteady behavior and heat transfer enhancement, still remain open. Previous studies of heat transfer in the grooved channel relevant for the present study were reviewed by Herman and Kang [11,13].

In a grooved channel the flow and thermal boundary layers successively develop along the heated surfaces of blocks protruding periodically into the main channel flow (Fig. 1(b)). The flow separates at the trailing edge of each block and then redevelops at the leading edge of the downstream block. It is well known that such periodic redevelopment of the thermal boundary layer is accompanied by high heat transfer coefficients [21]. However, at the same time warm fluid is trapped in the slow recirculating flow in the groove, where diffusion is the dominant heat transfer mechanism through the free shear layer spanning the groove [1,5–7,17]. Previous studies have shown that heat transfer along a groove-channel periodicity can be low due to this inefficient groove region [4,11,15,21]. Since the walls forming the groove represent a considerable portion of the total wetted area of the heated block or surface, their contribution to the overall heat transfer performance of the system is significant. Therefore, finding means of improving heat transfer from these walls is important when attempting to enhance heat transfer in grooved channels. Various heat transfer enhancement schemes, both active and passive, have been proposed in the literature [21].

The results reported in the paper are a part of a more comprehensive study of heat transfer and heat transfer enhancement in grooved channels. Heat transfer in the reference geometry, the asymmetrically heated parallel plate channel was compared with that in the basic grooved channel (BGC: heated blocks attached to one wall of the parallel plate or rectangular channel, [11]) and two enhanced configurations, the grooved channel with cylindrical eddy promoters [13] and vanes (displayed in Fig. 1(a) and reported in the present paper). The investigated approaches to heat transfer

* Corresponding author. Tel.: +1-410-516-4467; fax: +1-410-516-7254.

E-mail address: herman@titan.me.jhu.edu (C. Herman).

0017-9310/02/$ - see front matter
PII: S0017-9310(02)00092-3

Nomenclature

b	parameter for holographic interferometry
A	surface area, m^2
c_p	specific heat at constant pressure, J/kg K
C_f	friction coefficient, $C_f \equiv \tau_w/\frac{1}{2}\rho u_m^2$
D_h	hydraulic diameter, $D_h \equiv 4WH/2(W+H) =$ 0.0444 m
f	friction factor
h	heat transfer coefficient, $W/(m^2\ K)$
H	full channel height, 0.025 m
k	thermal conductivity, W/(m K)
L	periodicity length, 0.050 m
l	direction of the surface normal
$\dot{m}$	mass flow rate, kg/s
n	refractive index
Nu	Nusselt number
p	pressure, Pa
Po	Poiseuille number, $Po \equiv C_f Re$
q	heat transfer rate, W
q''	heat flux, W/m^2
Re	Reynolds number for the grooved channel, $Re \equiv (u_m D_h)/v$
S	fringe order
T	temperature, °C
u	velocity, m/s
W	spanwise dimension of the channel, 0.2 m
x	axial coordinate direction, m
X	total length in streamwise direction, m
y	heightwise coordinate, m
z	spanwise coordinate, m

Greek symbols

Δ	difference
λ	wavelength of laser light, m
ξ	streamwise coordinate, m
v	kinematic viscosity, m^2/s
ρ	fluid density, kg/m^3
τ_w	wall shear stress, N/m^2

Subscripts

b	refers to block, local value
ba	refers to block-average
eff	effective value
in	refers to inlet
l	laminar
m	mean value
out	refers to outlet
t	turbulent
ts	refers to test section
∞	refers to reference state

enhancement focused on the modification of the surface topography of the BGC, with the aim to trigger the early onset (at a lower Reynolds number) and amplify the amplitude of flow oscillations (in the BGC and the grooved channel with cylinders, GCC) as well as to redirect the flow into regions characterized by low heat transfer (grooved channel with vanes, GCV). The enhancement method considered in the present study falls into the class of passive methods favored in practical applications because of their simplicity, reliability and relatively low cost.

2. Background

During the past two decades, considerable attention has been devoted to the investigation of the role of flow destabilization in heat transfer enhancement. Resonant heat transfer enhancement was first introduced as active flow modulation in [1,5–7,17], and was shown to be effective in satisfying both heat transfer and pressure drop requirements. Studies show [1,2,10–12,15] that special periodic surface topographies, such as grooved, communicating or wavy channels, support passive flow modulation. The self-sustained oscillations that develop in these geometries lead to heat transfer enhancement without the need to apply active forcing. The magnitude of enhancement reported in these studies varied in a wide range, primarily depending on surface topography and boundary conditions.

Herman [10] and Herman and Kang [12] identified six characteristic regions in the grooved channel of interest in heat transfer enhancement studies. They are illustrated in Fig. 1(b), with the contours of the regions superimposed to the temperature fields visualized in the BGC and displayed as interference patterns (fringes correspond to isotherms). Herman and Kang [11,13] focused on resonant heat transfer enhancement in their analysis of the BGC and the GCC. The self-sustained oscillations improved heat transfer in regions II and III of the BGC. Above the Reynolds number characteristic for the onset of self-sustained oscillations, Re_c (BGC: $Re_c = 1050$ to 1300), heat transfer in the BGC was higher than in the reference geometry, the asymmetrically heated parallel plate channel. Considerable enhancement was accomplished in the GCC in the accelerating flow in region IV. The flow acceleration was accomplished by the addition of cylinders above the downstream edge of the heated blocks. Heat transfer in the GCC showed an increase by a factor of 1.2–1.8 when compared to the BGC. However, self-sustained oscillations did not lead to heat transfer enhancement in

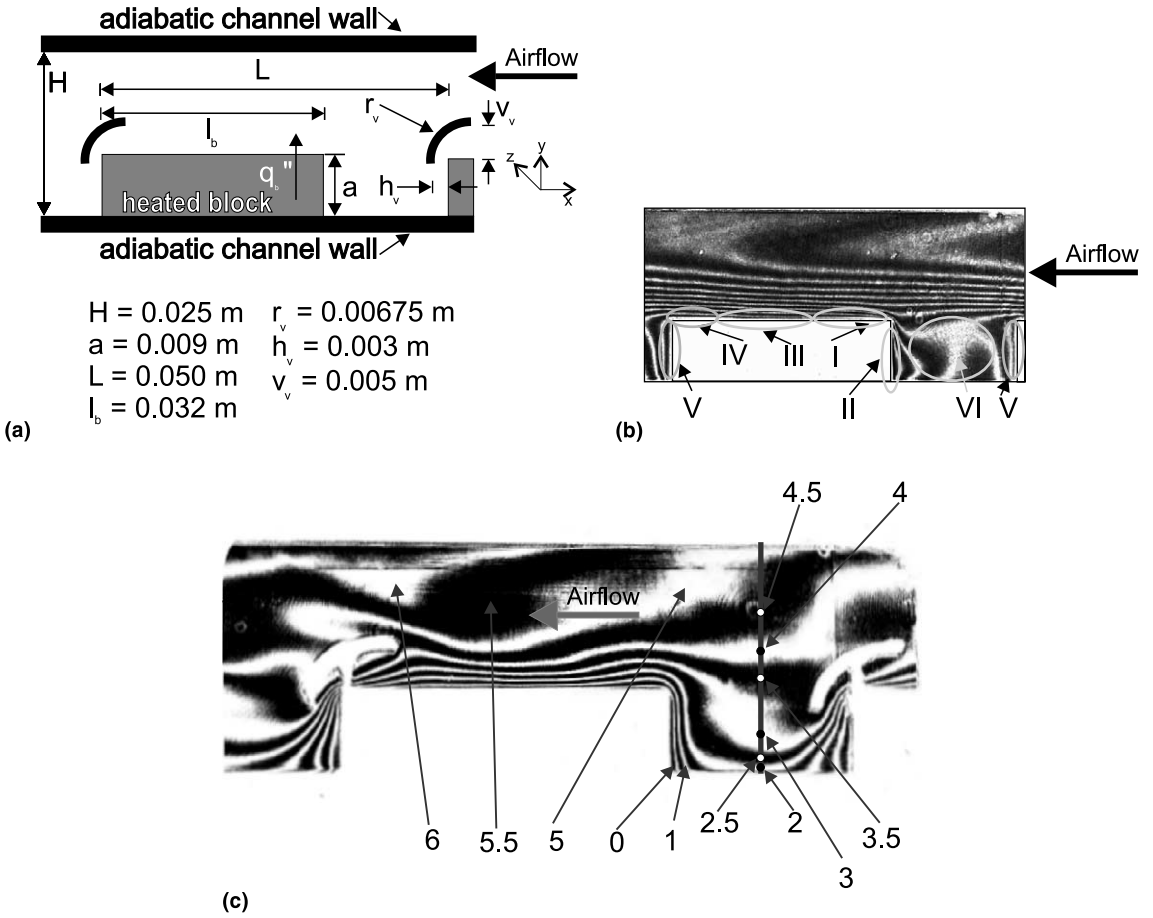

Fig. 1. (a) Schematic of the investigated channel geometry. (b) Visualization of temperature fields in the BGC through the interferometric fringe pattern recorded at $Re = 530$ with the six regions of interest for the characterization of heat transfer. (c) Fringes in the GCV at $Re = 530$ numbered as required in the reconstruction of temperature distributions from the interferometric fringe pattern.

region V, and the enhancement accomplished in region II was only moderate. These regions are targeted in the present study.

Heat transfer enhancement strategies for the grooved channel were compared in terms of overall heat transfer and pressure drop performance by Herman and Kang [12]. Previous papers [11,13] as well as the present study focus on the physical details responsible for the enhancement, and report local temperature distributions and heat transfer rates in addition to the inlet–outlet performance criteria, as discussed in [12]. The motivation for introducing curved vanes above the downstream edge of the heated block was to increase heat transfer along the downstream portion of the horizontal heated wall (region IV) as well as from the upstream (region II) and downstream (region V) vertical walls of the heated block. The vane accelerates the flow and deflects it into the groove, as illustrated in Fig. 1(a).

Vanes are commonly used to control the flow in pumps and turbines [18]. In pipes and ducts, in applications similar to the present study, they reduce flow separation and the associated flow losses. In grooved channels flow deflection allows a more aggressive removal of the hot fluid from the groove region. Anderson and Moffat [3] used curved vanes (which they called "scoops") to improve the cooling of discrete electronic components through increased thermal mixing in the coolant flow. In order to reduce air temperatures near electronic components, they installed small "scoops" on the bottom of the groove, in the regions of high temperature and low velocity. The "scoops" were oriented such to direct the flow out of the groove (as opposed to deflecting it into the groove, as in our study) with the aim to enhance mixing and reduce temperature nonuniformity. Anderson and Moffat [3] found that their approach induces smaller pressure drop than conventional turbulators for a given decrease of the operating temperature.

Our earlier studies of complex, self-sustained oscillatory flows in grooved and communicating channels

[2,10–12] demonstrated that holographic interferometry (HI) is a tool suitable for the study of high-speed convective heat transfer processes in transparent fluids. In the present study we visualize unsteady temperature fields in the grooved channel with curved vanes, GCV, using real-time HI combined with high-speed cinematography to measure temperature distributions and local heat transfer. At the same time we use temperature as tracer to evaluate the complex flow structures [9]. We describe the experimental hardware and the measurement technique in Section 4. Visualized and reconstructed temperature fields are discussed in Sections 5.1 and 5.2. Local heat transfer data for the GCV are compared with those for the BGC, and overall heat transfer and pressure drop data are presented in Sections 5.3 and 5.4, respectively.

3. Channel geometry and physical situation

The investigated channel geometry and the physical situation are presented schematically in Fig. 1(a). The geometry of the basic grooved channel (without the curved vanes), described in more detail by Herman and Kang [11], was guided by the geometry analyzed by Ghaddar et al. [5,6] and Patera and Mikic [17]. Key physical dimensions are indicated in Fig. 1(a). The curved vanes were manufactured by cutting a 13.5 mm diameter garolite tube into quarters. The vertical offset of the leading edge of the vane with respect to the horizontal block surface is $v_v = 5.2$ mm and the horizontal offset of the trailing edge of the vane with respect to the vertical wall of the heated block is $h_v = 3.3$ mm (Fig. 1(a)). A jet-like flow, with a discharge-to-inlet ratio of approximately 0.6, is formed between the heated block and the vane. The addition of the vane causes acceleration of the flow trapped by the vane and discharging into the groove.

4. Method of study

4.1. Experimental setup

Visualization experiments using HI were carried out in a wind tunnel that uses air as the working fluid. The design of the wind tunnel was discussed in more detail by Herman and Kang [11,12], and its photograph is displayed in Fig. 2(a). The wind tunnel, positioned horizontally, consists of the intake and exit nozzles and the three tunnel sections visible in Fig. 2(a). The 549 mm long upstream section, which is identical to the downstream section, allows a well-defined, reproducible velocity profile (in form very close to the fully developed profile) to develop by the time the flow reaches the test section. The downstream section prevents the influence of exit effects on the flow distribution in the test section. The exit nozzle, attached to the downstream section, converges to a hose with an inner diameter of 32 mm, which is connected to a rotameter and a draw-through blower. A control valve together with a bypass valve allow the experimenter to adjust the flow rate.

The test section is 508 mm long, $H = 25$ mm high and $W = 200$ mm wide. Ten equally spaced, electrically heated copper blocks are mounted on its bottom wall. The spanwise dimension of the test channel, $W = 200$ mm, was selected to yield approximately two-dimensional flow and temperature fields in the Cartesian coordinate system, which is a requirement for accurate measurements and relatively easy reconstruction of temperature profiles from fringe patterns obtained by HI. The spanwise dimension W also determines the number of fringes developing between the heated block and the adiabatic wall for a prescribed temperature difference between the two.

The transparent acrylic side walls of the experimental channel are inserted into grooves milled into the top and bottom walls. A glass window is glued into each side wall in the region of the ninth heated block, as required for interferometric measurements. Eight of the ten vanes are supported by the acrylic side walls. The vanes above the eighth and ninth blocks (in the visualization region) were each supported by four stiff, 0.6 mm diameter pins. Noise generation and vibration effects are always of concern in practical applications of oscillating flows. Since the vane configuration considered in the paper resembles louvered-fin geometries used to improve heat transfer in heat exchangers, the issues and solutions to noise and vibration problems in practical implementations of the investigated configuration are similar to those for the well-established louvered fins. Optimization of the vane geometry using numerical tools also offers the possibility to minimize noise and vibration effects.

The structure of the electrically heated copper blocks was described in previous publications of the authors [11], and only key information is provided here because of space limitations. Each block is $a = 9$ mm high, $l_b = 32$ mm long (in the streamwise direction) and $W = 200$ mm wide. Nine of the ten blocks are equipped with two T-type thermocouples (one close to the upstream edge and the other close to the downstream edge) mounted immediately underneath the block surface to measure surface temperatures. The ninth block, the one visible in the interferometric image, holds six thermocouples (immediately underneath the surface) that provide accurate reference temperature data for interferometric measurements. A resistive electric heater foil ($R = 33.7\ \Omega$) is bonded with adhesive into the 2.5 mm deep groove milled into the bottom surface of the block. Since the groove is deeper than the foil thickness, a layer of air separates the heater foil from the bottom wall of the test section. The heated block is in direct thermal

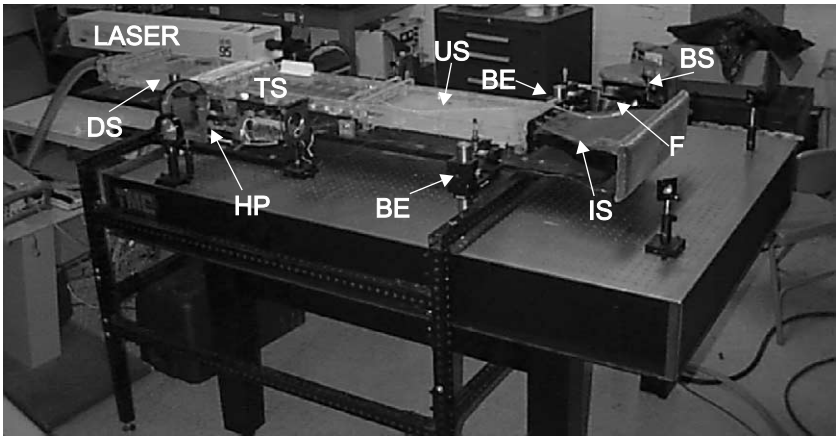

(a)

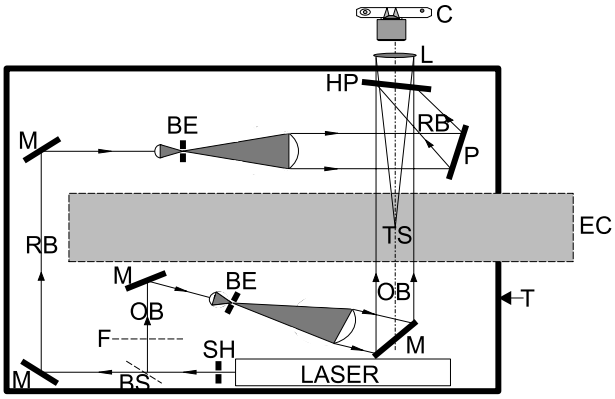

SH Shutter
M Mirror
F Filter
BS Beam splitter
BE Beam expander
P Adjustment mirror
HP Holographic plate
IS Intake section
US Upstream section
L Imaging lens
C Camera
T Optical table
RB Reference beam
OB Object beam
TS Test section
EC Experimental channel
DS Downstream section
E Exit nozzle

(b)

Fig. 2. (a) Photograph of the wind tunnel and the optical equipment assembled on the optical table. (b) Schematic of the optical arrangement for holographic interferometry.

contact with the bottom plane wall only through the narrow area around the groove, to minimize conductive losses. Constant power, 4.1–5.4 W/block, is delivered to the heater foil by an AC power supply. Average block temperatures varied between 30 and 75 °C in our experiments.

4.2. Boundary conditions

The top wall of the test section is manufactured of acrylic and the bottom wall of garolite (withstands higher temperatures), which are both low thermal conductivity materials. Such selection of test section materials leads to approximately adiabatic thermal boundary conditions on these walls. Losses through the side walls were neglected. The thermal boundary condition on the heated blocks is characterized by constant heat flux. Actual local heat flux values along the surface of the heated block were measured by HI (Sections 5.2 and 5.3). Thermal losses in the test section were both measured and estimated using a numerical model [11–13], and they served as reference data. The effect of conduction losses

from the heated blocks to the bottom wall was estimated from the energy balance on the test section. The overall heat transfer rate from all 10 blocks to the air by convection, q, was found as

$$q = \dot{m} c_p (T_{out} - T_{in}). \quad (1)$$

The outlet and inlet temperatures, T_{out} and T_{in} in Eq. (1), were measured by thermocouples, and the mass flow rate, $\dot{m}$, by rotameters. The energy delivered to the heated blocks was monitored by measuring the potential difference developing across the resistive heaters. More details regarding the verification of the thermal boundary conditions are available in [11–13].

Above a critical Reynolds number and at a sufficient downstream distance, a periodic fully developed flow regime is established in the test section, as shown by Amon and coworkers [2,4,17]. This regime is the focus of our visualization experiments, since the instantaneous velocity and scaled temperature fields repeat periodically in space. We consider one channel geometric periodicity length L, that consists of a one groove and block unit (Fig. 1(a)), located in the region of the ninth heated block.

4.3. Instrumentation

The temperatures of the channel ceiling and heated blocks are monitored by T-type thermocouples. Sample thermocouples were tested, and uncertainties in temperature measurements were determined to be ±0.3 °C. Inlet and outlet temperatures of the coolant are measured using batteries of six T-type thermocouples to increase measurement accuracy.

Pressure taps at the inlet and outlet of the test section, linked to a Hook Gage type manometer (uncertainties: ±0.06 Pa), are used for pressure drop measurements. A second Hook Gage manometer and a pressure transducer were available to verify pressure drop data. Two rotameters are used to measure volume flow rates in the low ($Re = 200$ to 2110) and high ($Re = 2110$ to 6580) Reynolds numbers regimes. The Reynolds number definition, $Re \equiv u_m D_h / \nu$, is based on the hydraulic diameter D_h (defined for the cross-section $H \times W$), and the mean velocity, u_m. The mean air flow velocity u_m is specified over the free channel cross-section $H \times W$. Based on manufacturer specifications for rotameter uncertainty, the uncertainties in the measured Reynolds numbers are 3.1% at $Re = 2110$ and 2.0% at $Re = 6580$ for the low- and high-range rotameters, respectively. The reader is referred to previous publications [11–13] for more details regarding the instrumentation.

4.4. Experimental method

Real-time HI was used to visualize the unsteady temperature fields in the GCV in the form of isotherms. Interferometric fringe patterns were recorded by a rotating prism high-speed film camera at rates between 1000 and 2000 picture frames per second. The optical arrangement used in the interferometric measurements is shown schematically in Fig. 2(b). The light source is a 0.8 W Argon–Ion laser. The laser beam is divided into the reference beam (RB) and the object beam (OB) by means of a beam splitter (BS). Both beams are then expanded into parallel light bundles by the beam expanders (BE). The object beam passes through the test section (TS) with the phase object (generating the refractive index field to be related to temperature in the reconstruction phase, Section 5.2), and then falls on the holographic plate *HP*. The reference beam falls directly onto the holographic plate.

Visualization is carried out in two steps. The reference state (usually with the fluid in the measurement volume at ambient temperature $T(x,y) = T_\infty$ with the corresponding refractive index n_∞) is recorded first. Next, the holographic plate is processed, and then accurately repositioned into the precision plate holder. In the second step, the reference state of the investigated object is reconstructed by illuminating the holographic plate with the reference beam. At the same time, the investigated physical process is activated, i.e., heating of the blocks in the test section commences. The heating changes the refractive index of the fluid in the test section ($n \neq n_\infty$), and, consequently the object wave experiences a phase change on its way through the test section. The difference between the reference state recorded earlier and the current state of the fluid in the measurement volume, manifested as a phase shift in the OB, is visualized in the form of an interference fringe pattern (Figs. 1(b) and (c)). Interferometric images shown in this paper were all recorded using the infinite fringe field alignment [8,9].

In the reconstruction process interferometric images were scanned, digitized with resolutions of 600 pixels × 250 pixels, and evaluated quantitatively using digital image processing tools [13]. Since the spatial resolution of the film material is very high, the scanning resolution can be increased easily, if required. Locations of interferometric fringes (light intensity minima and maxima in the fringe pattern) were measured at consecutive cross-sections in the ninth block-groove region. The orientation of the fringes in the groove can be both horizontal and vertical, and this requires the measurement of both horizontal and vertical cross-sections to accurately detect fringe locations. One vertical cross-section in the region of the groove is illustrated in Fig. 1(c). Each fringe is assigned a number $S = S(x,y)$, called the fringe order (Fig. 1(c)). The number $S = 0$ is assigned to the bright fringe at the reference temperature T_b (measured by the thermocouples immediately beneath the surface in the middle of the block, Section 4.1). The fringe labeled "0" is visible in region II, it bends around the

block and follows the horizontal surface (region I) to blend into the block near its middle, where T_b is measured. The bright fringes are numbered $S = 1, 2, 3 \ldots$, whereas the dark fringes are assigned the orders $S = 0.5, 1.5, 2.5, \ldots$, as illustrated in Fig. 1(c). Increasing fringe orders correspond to decreasing temperatures. The equation of ideal interferometry, $S(x,y) \cdot \lambda = [n(x,y) - n_\infty] \cdot W$ describes the phase shift of laser light of wavelength λ (514.5 nm) along the optical path of length W caused by the change of the refractive index from n_∞ (for ambient conditions at the time of holographic exposure) to $n(x,y)$ (during the measurement). The temperature distribution is recovered as

$$T(x,y) = \frac{T_b}{1 + b(T_\infty)S(x,y)} \quad \text{with}$$
$$b(T_\infty) \equiv \frac{\lambda}{W(n_\infty - 1)}. \tag{2}$$

The parameter b accounts for the complex influence of fluid pressure, temperature and fluid properties at reference conditions as well as the properties of the light source as discussed in [8,20].

Additional temperatures, indicated by thermocouples flush-mounted in the ceiling of the test section, complement the block thermocouple data, and they allow the estimation of the uncertainties of temperature measurements by HI. The temperature measurement uncertainty in the investigated channel is estimated to be around 3%, mainly caused by uncertainties in the reference temperature measurement with a modest contribution due to the reconstruction method. More details regarding the uncertainties of temperature measurements in the grooved channel are available in previous publications of the authors [11–13]. General information regarding HI [8,20] and specific information on the optical setup used in our experiments is also available in the literature [8,9].

5. Results and discussion

5.1. Visualized temperature fields

Temperature fields were visualized for Reynolds numbers in the range $Re = 200$ to 2370. Instantaneous temperature fields in the BGC and the GCV, visualized by HI in the form of fringe patterns at $Re = 530$, 1580 and 2370, are displayed in Fig. 3. The temperature difference for a pair of fringes is approximately 2.8 K.

We found that the transition from steady to oscillatory flow occurs around $Re_c = 450$ in the GCV, contrasted to $Re_c = 1050$ to 1300 for the BGC. The oscillations in the GCV are accompanied by traveling waves in the main channel flow at low to intermediate Reynolds numbers (Fig. 4(e)); the waves cannot be discerned at higher Re (Fig. 3(c)). The traveling waves are more pronounced in the GCV than in the BGC [11]; they are illustrated for $Re = 530$ in Fig. 4(e) and contrasted to the steady state situation in the BGC at the same Reynolds number in Fig. 4(d). It has been shown that the wave structures in the BGC are characteristic of the Tollmien–Schlichting waves, which are activated by the Kelvin–Helmholtz instabilities of the free shear layer spanning the groove [2,5,6,11]. The flow oscillations in the GCV are mainly caused by flow separation from the tips of the vanes. The traveling waves in the main channel cause a periodic local compression and expansion of the thermal boundary layer on the top surface of the heated block (regions I, III and IV in the BGC and regions I and III in the GCV) that we call the "massaging" effect. The subtle local variations of the temperature gradient induced by the waves contribute somewhat to the heat transfer enhancement in the GCV, and were found to be the key mechanism of enhancement in the BGC [11]. Oscillations contributing to heat transfer enhancement were also detected in region II in the BGC. Such oscillations do not develop in the investigated geometry, the GCV.

Although the flow situation changes with increasing Re, certain characteristic phenomena are present in all images in Fig. 3, and these are discussed first. The key feature observed in the fringe patterns in the BGC (top image of the pairs in Fig. 3) is the redevelopment of the thermal boundary layer in regions I–III. It is accompanied by high fringe density (Figs. 1(b) and 3), which indicates high temperature gradients and heat transfer rates. This redevelopment of the thermal boundary layer is observed at all Reynolds numbers. As expected, the thermal boundary layer thickness decreases, i.e., the fringe density and the heat transfer rate increase, with increasing Re. As the flow moves along the top surface of the heated block from region I to III and IV, the thermal boundary layer thickness increases in the BGC, which leads to decreasing heat transfer rates. Fringes emerging from the horizontal surface of the heated block in both channel geometries indicate nonuniform (increasing) temperatures along the block surface, which is consistent with the constant heat flux boundary condition. The fringe density in the BGC is low on the vertical walls of the block in regions II and V. The wide isotherms in the groove in regions V and VI form as the result of the slow, recirculating flow in the groove and they show little dependence on Re. The images in Fig. 3 indicate that HI is suitable for visualization of flow structures (by means of isotherms) in the main channel [9], as the scaled velocity and temperature profiles are similar in regions I, III and IV. However, due to loss of similarity, isotherms do not reflect the flow structure in the recirculation regions (region VI in the BGC and region I in the GCV) as the temperature profile shows a monotous decrease from groove wall temperature to test

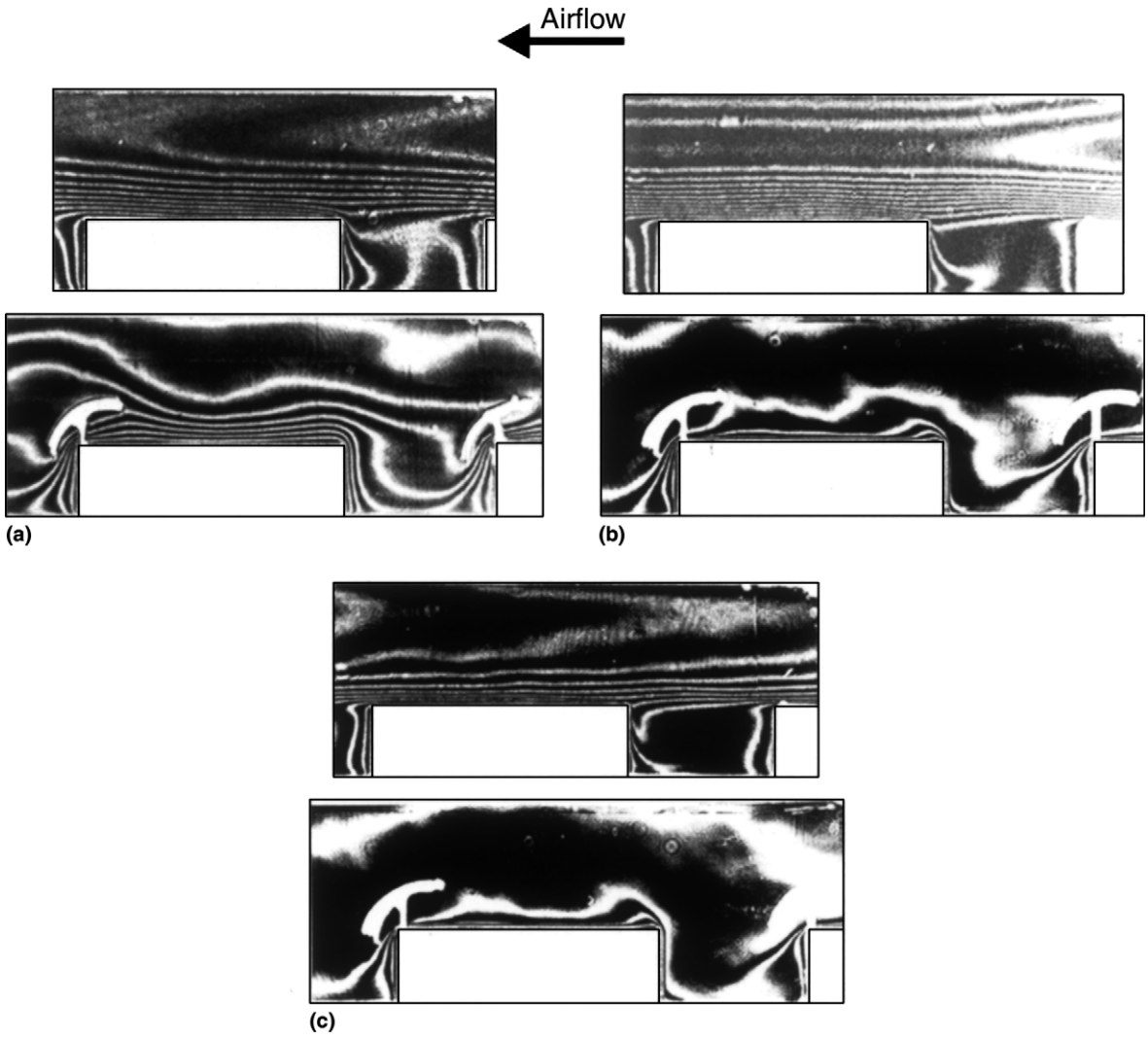

Fig. 3. Visualized temperature fields in the form of interferometric images for the BGC and the GCV at (a) $Re = 530$, (b) 1580 and (c) 2370.

section ceiling temperature, whereas the shape of the velocity profile is much more complex and can include a change of sign in case of flow reversal.

To remedy the problem of poor heat transfer from the vertical walls of groove (regions II and especially V), curved vanes were mounted above the trailing edge (region IV) of the block (Fig. 1(a), Section 3). As a result, we observe a dramatic compression of isotherms in regions IV, V and VI (Figs. 4(a) and (b)) in the GCV when compared to the BGC. The shape of the isotherms in region II changes too (Fig. 3(a)), due to the change of the flow structure in the groove region (recirculating flow in the BGC versus the jet-like flow formed between the vane and the heated block in the GCV). Conversely to the BGC, the temperature gradients in regions II, V and VI in the GCV exhibit a strong dependence on Re (Fig. 3). Increased fringe density, leading to increased temperature gradients, is also visible in region IV, caused by the flow accelerating under the vane (Fig. 3). This enhancement is also present at higher Reynolds numbers. Another apparent difference between the two channels is observed in region I (Fig. 4(c)), where the thickness of the thermal boundary layer increases in the GCV (in particular at higher Re), a feature that suggests the presence of a separation bubble (barely visible at $Re = 530$, Fig. 3(a), and prominent at $Re = 1580$, Fig. 3(b), as well as at $Re = 2370$ in Figs. 3(c) and 4(c)). The jet from underneath the vane discharges onto the leading vertical wall of the heated block and the resulting boundary layer formed in region II is unable to remain

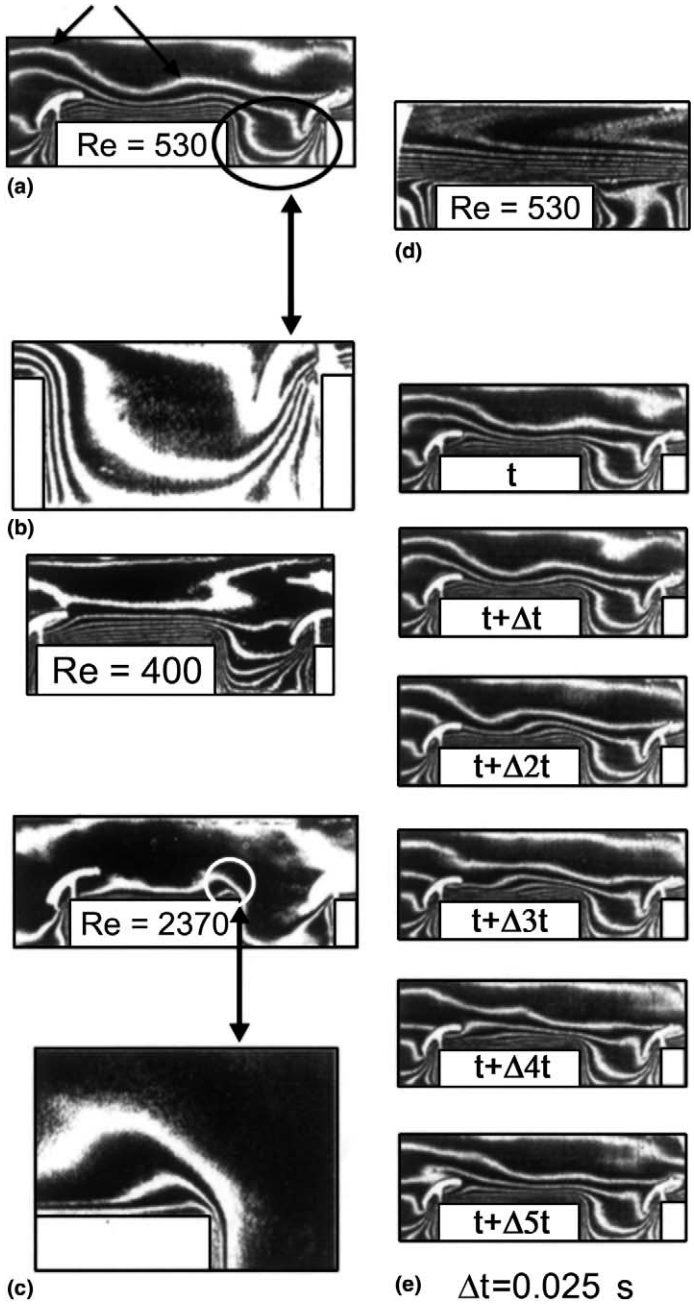

Fig. 4. Characteristic features of the interferometric images in the GCV: (a) waves propagating in the main channel; (b) high temperature gradients in the groove region; (c) flow separation at the leading edge of the block; (d) steady flow in the BGC with low isotherm density along the vertical walls contrasted to the (e) time evolution of unsteady temperature fields in the GCV for $Re = 530$.

attached on the block surface as the air flows around the sharp corner of the block. Separation along blunt objects, such as in region I indicated by the encircled portion in Fig. 4(c) (top) and the magnification in Fig. 4(c) (bottom), is manifested as the local widening of the thermal boundary layer (that can be visualized in the interferometric image) in the region of flow separation (recirculation bubble). This widening is caused by the lowering of temperature gradients in the fluid in the vicinity of the surface caused by the lower flow velocities. This widening of the isotherms in the developing boundary layer was shown to be indicative of flow

separation in other forced convection situations as well [9]. The shape of the isotherms indicates that in the investigated channel geometry, the GCV, the temperature gradients are high and of similar magnitude along the entire wetted surface of the heated block – with exception of region I – and their magnitude exhibits only a weak time dependence. Therefore, the mixing of the warm groove fluid with the bulk flow is essentially continuous GCV as opposed to periodic and strongly influenced by the self-sustained oscillations in the BGC. In the BGC the high isotherm density is mainly limited to regions I and III.

5.2. Reconstructed temperature fields

With HI it is possible to quantitatively reconstruct the two-dimensional temperature fields from the instantaneous isotherm distributions captured on film during experimentation (Figs. 3 and 4) using the approach described in Section 4.4. Reconstructed temperature fields in the BGC and GCV for $Re = 530$ and 1580 are shown in Fig. 5. The temperature fields for the BGC quantitatively mirror the behavior patterns described when discussing the fringe pattern (Section 5.1), such as the redevelopment of the thermal boundary layer as well as increasing thermal boundary layer thickness and block surface temperature with increasing streamwise distance from the leading edge of the block (Figs. 5(a) and (c)).

The addition of the curved vanes causes a number of changes in the temperature fields (Figs. 5(b) and (d)). The difference is most pronounced in regions II and V, where the temperature gradients increase considerably. As a consequence, the temperature in region VI is lower in the GCV than in the BCG for a particular Re. The thermal boundary layers are thinner in the GCV (especially in region IV), with the exception of region I (where the recirculation bubble forms at higher Re, Fig. 4(c)). For the same Re, the region of the main channel flow with lower fluid temperatures is wider in the GCV than in the BGC.

Reconstructed temperature profiles at characteristic cross-sections along the surface of the heated block in the BGC and the GCV are shown in Fig. 6 for $Re = 530$. The temperature profiles in Fig. 6(a) are representative of vertical cross-sections in the main channel (regions I, III, and IV). Temperature gradients in region I (Fig. 6(a)) are larger in the BGC than in the GCV, indicative of higher heat transfer rates from the block surface to the bulk flow in the redeveloping thermal boundary layer. Another indication of boundary layer development in the BGC is the decreasing slope of the temperature profiles accompanied by increasing surface temperature with increasing downstream distance (regions I, III and IV). The lower temperature gradient at the leading edge of the block (region I) in the GCV is a consequence of low flow velocities in the recirculating flow in the separation bubble.

In Fig. 6(b), temperature profiles measured at three horizontal cross-sections along the upstream vertical wall (regions II and V of the upstream groove) are plotted. The temperature profiles were obtained for the entire length of the upstream groove. The shapes of the profiles exhibit similarities for the two geometries, characterized by higher temperature gradients at both walls and a relatively flat minimum in the middle of the

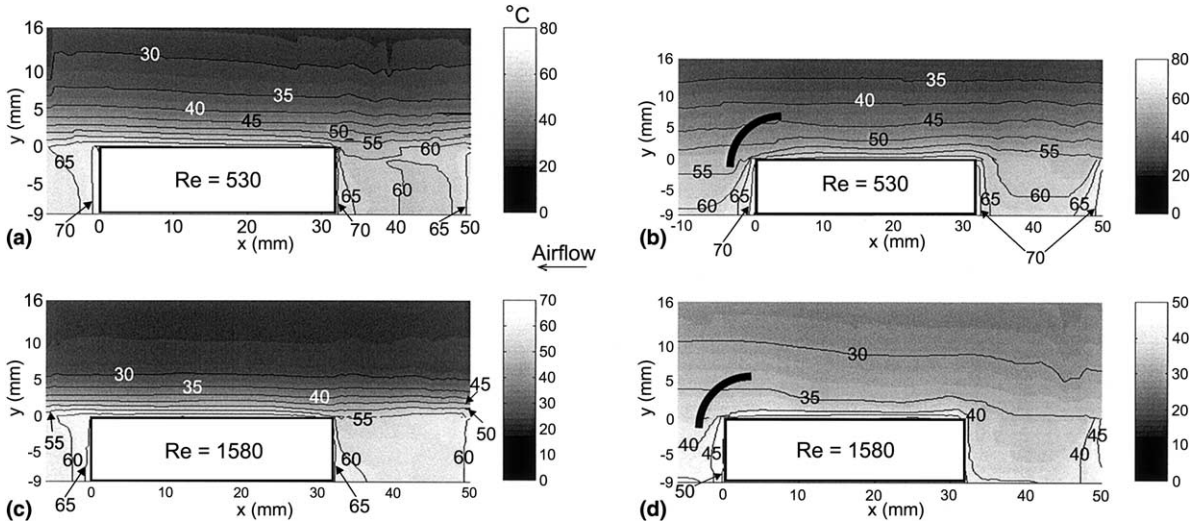

Fig. 5. Temperature fields reconstructed from the interferometric images displayed in Fig. 3 at $Re = 530$ (a) in the BGC and (b) GCV as well as at $Re = 1580$ (c) in the BGC and (d) GCV.

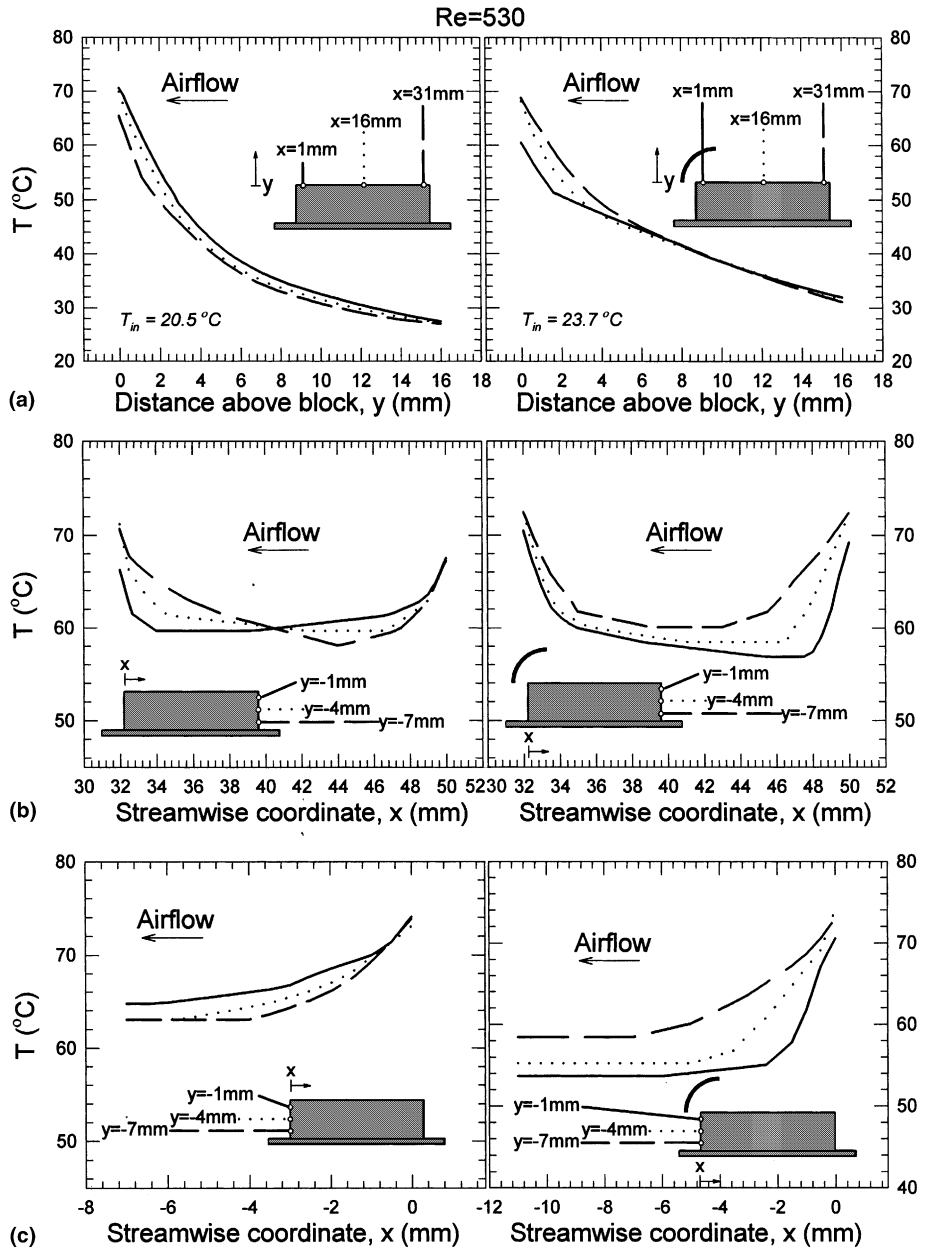

Fig. 6. Reconstructed temperature profiles at representative cross-sections for $Re = 530$ in the BGC (left) and GCV (right) along the (a) top horizontal surface, (b) upstream and (c) downstream vertical wall of the ninth heated block.

groove. The lower temperature region in the middle of the groove is wider and flatter in the GCV. Temperature gradients are higher at the portion of the wall close to the main channel in both channel geometries. At the same cross-section and *Re*, the temperature gradients at the walls are higher for the GCV, due to the higher flow velocities in the portion of the flow redirected into the groove by the vane, which then forms a boundary layer along region II. The temperature gradients in the BGC are higher in region II than in region V, due to the vertical velocity components caused by the flow oscillations in the upper portion of region II [11].

In Fig. 6(c) temperature profiles measured at three horizontal cross-sections along the downstream vertical wall, in region V, are displayed. Because of the limitations of viewing region in the interferometric visualization experiments, temperature profiles were obtained for a portion of the downstream groove only. The shapes of

the profiles and the results are similar to those discussed for Fig. 6(b), region V. The average temperature level in the downstream groove is higher in both channels because of the temperature rise in the fluid along block nine.

From the temperature data recovered from interferometric fringe patterns, temperature gradients along the surfaces of the heated block and local heat fluxes are determined. These heat fluxes serve as base for the local heat transfer analysis, rather than the heat flux data derived from the electric power measurements (corrected by estimating the thermal losses in the test section) that serve as reference values only.

5.3. Heat transfer

The heat transfer characteristics of the GCV were quantified and compared with those of the BGC and the asymmetrically heated parallel plate channel, by considering the Nusselt number behavior. The block-average heat transfer coefficient, h_{ba}, was determined first as

$$h_{ba} \equiv \frac{q_{ba}}{A_b(T_{ba} - T_m)} \tag{3}$$

and it is based on the heat flux $q''_{ba} = q_{ba}/A_b$ from the wetted surface area of the heated block to the cooling air. A_b is comprised of the upper horizontal surface and the vertical side walls. In the experiments discussed in the paper, the heat fluxes from the block to the cooling air were $q''_{ba} = 170$ and 194 W/m^2 for the BGC and the GCV at $Re = 530$, respectively, and at $Re = 1580$ they were $q''_{ba} = 241$ and 335 W/m^2. The block-average temperature T_{ba} is determined as the average of the upstream and downstream block thermocouple readings, and it is a time-averaged value. The bulk air temperature above each block T_m was calculated assuming a linear temperature rise along the test section, and it is based on the inlet and outlet temperature readings T_{in} and T_{out}. This definition of the mean temperature T_m was chosen rather than the commonly used mixing cup temperature because of the practical difficulties in determining the mixing cup temperature in the unsteady flow rich in recirculating regions. The assumptions regarding T_m, q_{ba}, heat losses and thermal boundary conditions were discussed and justified in previous publications of the authors [11–13].

With h_{ba} found using Eq. (3), the block-average Nusselt number Nu_{ba} is determined as

$$Nu_{ba} \equiv \frac{h_{ba} D_h}{k}. \tag{4}$$

The measured values of Nu_{ba} for the BGC, GCV and the computed results for the parallel plate channel are presented in Fig. 7(a) for $Re = 530$, 790, 1580 and 2370 as a function of the streamwise distance ξ. ξ is measured from test section inlet, from a location 9 mm upstream of the first heated block. The parallel plate channel values were computed assuming fluiddynamically fully developed and thermally developing laminar flow and using the approach described by Shah and London [19]. The thermal boundary condition on the heated wall of the parallel plate channel was specified by constant heat flux, same as in the grooved channels, and the opposite wall was adiabatic. The surface areas of the parallel plates in the analysis were identical to the total wetted area of the heated blocks in the grooved channel. Consequently, the size of the area subjected to the constant heat flux boundary condition was the same for all three channel configurations. The Nu_{ba} values displayed in Fig. 7(a) were obtained by averaging experimental data from a series of experiments. The estimated average experimental uncertainty in the determination of the

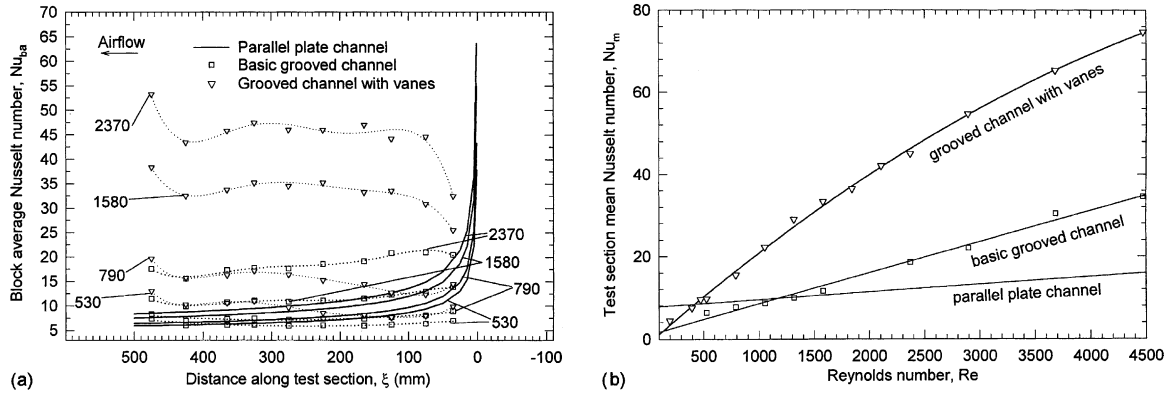

Fig. 7. (a) Measured block-average Nusselt numbers Nu_{ba} along the grooved channels with and without vanes and the computed local Nusselt number Nu along the parallel plate channel versus axial distance ξ for $Re = 530$, 790, 1580 and 2370. (b) Measured channel-average Nusselt numbers Nu_m for the two investigated surface topographies of the grooved channel and computed values for the parallel plate channel as function of the Reynolds number, Re.

block-average Nusselt number Nu_{ba} is 6%, a function of the uncertainties in measurement of the block and air temperatures.

The solid lines in Fig. 7(a) illustrate the Nusselt number behavior along the parallel plate channel. Boundary layer development, characterized by high Nusselt numbers, is recognized at the test section inlet. This feature is less pronounced for the BGC. The apparent difference between the BGC, parallel plate channel and the GCV is the low Nu_{ba} on the first block of the GCV caused by the flow separation in region I. A comparison of the parallel plate channel values with data for the BGC indicates that the measured Nu_{ba} at Reynolds numbers below the onset of self-sustained oscillations (BGC: $Re_c = 1050$ to 1300) are low and the flat plate has superior heat transfer performance over the entire channel length [11]. Heat transfer rates are moderately higher in the BGC than in the parallel plate channel for $Re = 1580$ and considerably higher at $Re = 2370$. Nusselt numbers downstream of the second heated block in the GCV are higher than in the parallel plate channel for all Re considered in Fig. 7(a). Heat transfer enhancement in the GCV is present at low Re and in the absence of oscillations (GCV: $Re_c = 450$ to 530) as the increased temperature gradients on the vertical surfaces of the block are not caused by flow oscillations. At $Re = 1580$ and 2370, the experimentally determined Nusselt numbers for the GCV are roughly 2.5–3.5 times the magnitude of those determined for BGC at the same Re. In both grooved channel configurations, the block-average Nusselt numbers are higher at the last block than upstream of this location, because the air immediately downstream of the last block is heated by one block only, which results in better heat removal. Results presented in Fig. 7(a) indicate that Nu_{ba} typically reaches a constant value by the location of the third block, which verifies that thermally fully developed conditions were achieved in the viewing region (on the ninth block), as required by the visualization part of our study.

To further clarify the differences in thermal performance between the three geometries and explore the role of flow velocity in heat transfer enhancement, heat transfer rates were recast in terms of the mean Nusselt number for the entire test section Nu_m. The mean Nusselt number for a given Reynolds number is determined as

$$Nu_m = \frac{1}{X_{ts}} \int_0^{X_{ts}} Nu_{ba}(\xi)\, d\xi. \tag{5}$$

X_{ts} in Eq. (5) refers to the length of the test section. Nu_m is plotted as function of the Reynolds number in Fig. 7(b). Experimental values for the BGC and GCV are compared with computed data for the parallel plate channel. The measured data for the BGC displayed in Fig. 7(b) intersect the parallel plate line around $Re \approx 1200$, and this value coincides roughly with the onset of flow oscillations in the BGC. This observation is consistent with the block-average Nusselt number behavior illustrated in Fig. 7(a). The line representing data for the GCV intersects the parallel plate line at a significantly lower Reynolds number, $Re \approx 400$, which also matches the results presented in Fig. 7(a).

After evaluating the overall heat transfer performance of the investigated channel geometries, we explore the mechanisms responsible for heat transfer enhancement by analyzing the local Nusselt number behavior. The local Nusselt number is defined as

$$Nu \equiv \frac{D_h \cdot (dT/dl)}{T_b - T_m}. \tag{6}$$

In Eq. (6), the l direction is normal to the heated surface of the block and the local temperature gradient dT/dl is measured by HI. T_b in Eq. (6) is the local surface temperature of the block determined from interferometric temperature data. The mean temperature of the air T_m at the vertical cross-section for which the local Nusselt number is determined was used as the reference value in Eq. (6). Two mean temperatures T_m, corresponding to the locations of the upstream and downstream vertical walls, respectively, were used in the determination of Nu for the two sets of horizontal cross-sections [13].

Images obtained by HI at $Re = 530$ and $Re = 1580$ were evaluated for both the BGC and the GCV, and the measured local Nusselt number data are contrasted in Fig. 8. 89 cross-sections (normal to the wetted surfaces of the ninth heated block) were analyzed for each image. At each cross-section, the temperature gradient at the block surface, dT/dl (required in Eq. (6)) was determined using a least squares polynomial fit applied to the temperature data points near the wall. The data are available in the measured temperature profiles, such as those shown in Figs. 5 and 6. More details on the steps in the determination of Nu and measurement uncertainties are available in previous publications of the authors [11,13]. To allow for easier interpretation of measurement data, the results shown in Fig. 8 are presented in a geometry specific coordinate system, where the wetted surfaces of the block are "unwrapped" along the x-axis. The coordinate $x = -9$ mm indicates the point where the downstream wall of the block meets the floor of the channel (bottom of the downstream groove). The location $x = 0$ mm corresponds to the trailing edge of the horizontal top surface that extends up to the leading edge at $x = 32$ mm. At this point, the upstream vertical wall of the block begins, and it ends at $x = 41$ mm, on the floor (bottom) of the channel in the upstream groove.

In the BGC the temperature gradients along region V are small and relatively independent of the Reynolds

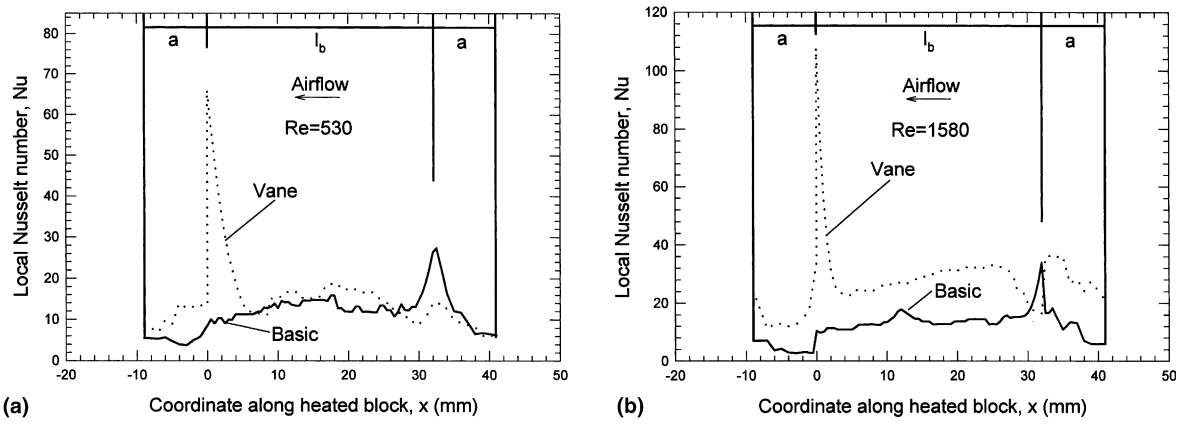

Fig. 8. Measured local Nusselt numbers Nu along the exposed surfaces of the ninth heated block shown as function of the geometry specific coordinate x at (a) $Re = 530$ and (b) 1580 for the BGC and the GCV.

number, which is reflected in the values of the local Nusselt number. Along regions I and II, 24 mm $< x <$ 36 mm (top of the upstream vertical wall and the leading edge portion of the horizontal surface), the local Nusselt number is larger than along any other portion of the block of the BGC. This is due to the redevelopment of the thermal boundary layer (region I) and the vertical velocity components induced by flow oscillations (region II). Heat transfer rates in region I of the GCV are lower because of the separation bubble. Since the separation region covers a relatively small portion of the wetted surface area, its effect on the block-averaged Nusselt number is not significant. In the GCV, the combination of the traveling waves in the main channel (region III) massaging the thermal boundary layer and flow acceleration in region IV (at approximately 0 mm $<$ $x < 6$ mm) result in higher local Nusselt numbers, as illustrated in Fig. 8. Towards the bottom of the upstream vertical wall (36 mm $< x <$ 41 mm) the benefits of flow deflection prevail in the GCV, especially at high Re. Overall, Nu increases with increasing flow velocities in the GCV. The improvements achieved on the vertical walls are dominant for the overall enhancement in the GCV, whereas the massaging of the thermal boundary layer is less significant.

The uncertainties in the measurement of Nu can be related to two sources. One of the sources is the fitting of the polynomial to temperature data points close to the heated surface. This allows the determination of the temperature gradient $\mathrm{d}T/\mathrm{d}l$ as well as the local temperature of the block surface T_b (by extrapolation), both required in Eq. (6). Errors were reduced by fitting a second-order polynomial with increasing number of data points first, then comparing these results, and selecting the fit that minimizes the influence of the number of data points. The second source of uncertainties is associated with the measurement of T_m. The estimated uncertainty in the measurement of Nu, obtained using a standard approach for the propagation of errors, is 7–9% [13].

The measured local Nusselt number profiles shown in Fig. 8 were integrated along the wetted surface of the block to determine their average value $\overline{Nu}$. For the BGC the values of $\overline{Nu}$ (determined using HI) were found to be 11.5 and 13.3 at $Re = 530$ and 1580, respectively. For the GCV these values were 14.9 and 27.1, respectively, at the same Reynolds numbers. The differences between the optically determined $\overline{Nu}$ and the non-optical values Nu_{ba} displayed in Fig. 7(a) can be attributed to several factors. First, when determining Nu_{ba} (Fig. 7(a)), the mean temperature of the block T_{ba} in Eq. (3) was the arithmetic average of the thermocouple readings recorded by the six thermocouples imbedded in the ninth heated block. Thermocouples in this setting deliver the time-averaged value of the copper block temperature, and T_{ba} is the spatially averaged value assumed to be representative of the entire block. For $\overline{Nu}$ block temperatures T_b and the temperature gradients $\mathrm{d}T/\mathrm{d}l$ were unique at each point along the block surface. These temperature data are representative of the time instant when the interferogram was recorded. In the non-optical Nusselt number measurement, the temperature of the air at the cross-section above the centerline of the block was taken as the representative value for T_m in Eq. (3). As previously discussed, values of T_m used in the determination of Nu (Eq. (6)) over the horizontal block top surface are representative of the individual cross-section considered. From the discussion it follows that the spatially averaged Nusselt number value $\overline{Nu}$ – determined by spatial integration of Nu for a particular time instant – is not necessarily identical to the time-averaged value of the Nusselt number Nu_{ba} averaged for the same spatial domain. Therefore, their direct comparison is not an adequate measure of the experimental uncertainty in

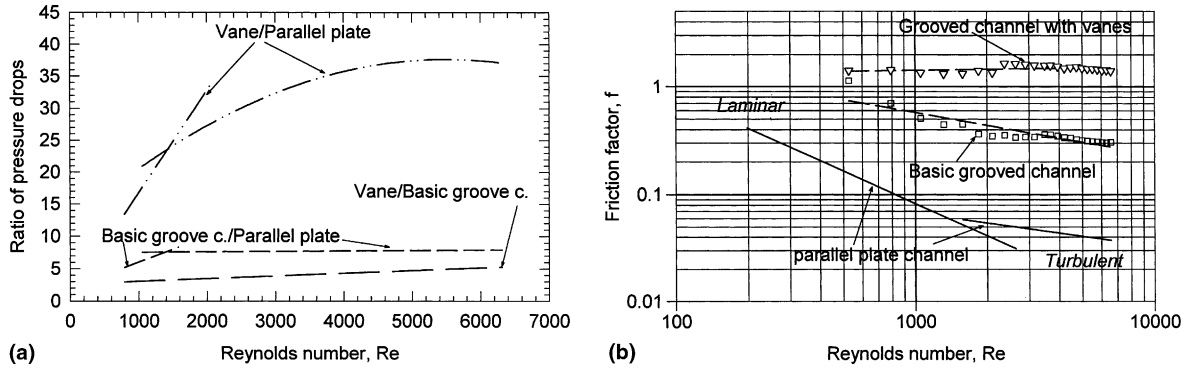

Fig. 9. (a) Ratio of the measured pressure drops for the grooved channels with and without vanes to the computed pressure drops for the parallel plate channel and (b) measured and computed friction factors for the three situations considered as function of the Reynolds number.

the determination of either Nusselt number [13] and can only serve as general reference.

5.4. Pressure drop

The pressure drop accompanying the heat transfer enhancement caused by the modification of the channel geometry is a key criterion when evaluating the overall performance of the system. Pressure drops Δp in the BGC and the GCV were measured along the test section and compared with predictions for a channel with rectangular cross-section characterized by an aspect ratio $H : W = 0.125$. Friction factors for the rectangular channel in the laminar regime [16] f_l were found as

$$f_l = \frac{82.34}{Re}. \tag{7}$$

Friction factors for the rectangular channel in the turbulent regime f_t were found implicitly using the Colebrook equation [14]

$$\frac{1}{\sqrt{f_t}} = 2\log_{10}(Re_{\mathrm{eff}}\sqrt{f_t}) - 0.8. \tag{8}$$

In order to find Re_{eff} we take advantage of values of the Poiseuille number, defined as

$$Po \equiv C_f Re \tag{9}$$

reported in the literature. For the aspect ratio H/W characterizing the cross-section of the experimental channel the value of the $Po = 20.6$ and for the circular channel it is $Po = 16$ [22]. By substituting these two values into Eq. (9), we find D_{eff}, required to determine the modified Reynolds number $Re_{\mathrm{eff}} \equiv u_m D_{\mathrm{eff}}/v$ for Eq. (8), following the approach described in [22].

To evaluate the relative pressure drop performance of the three channel geometries, the ratio of the measured pressure drop for the two grooved channels to the pressure drop in the rectangular channel is presented in Fig. 9(a). The measured pressure drop in the BGC and GCV, is up to 8 and 38 times higher, respectively, than in the rectangular channel. The pressure drop in GCV is approximately 3–5 times higher than in the BGC for the investigated range of flow velocities. The values presented in Fig. 9(a) suggest that below a certain Reynolds number, for $Re < 1000$, the pressure drop penalty in the GCV is only moderately higher than for the BGC. Thus we conclude that operating regimes in this lower Reynolds number range are favorable for the GCV.

Friction factors for the investigated grooved channels were determined from the pressure drop measurements Δp as

$$f \equiv \frac{\Delta p}{(X_{\mathrm{ts}}/D_{\mathrm{h}})(\rho u_m^2/2)}. \tag{10}$$

The measured friction factors as function of Re are presented in Fig. 9(b). Fig. 9(b) indicates that the GCV has the least favorable pressure drop (as well as the most favorable heat transfer) performance of the three investigated channel geometries.

5.5. Overall performance

We use the ratio of the measured channel-average Nusselt number Nu_m (relative to the corresponding value for the PPC) and the friction factor (again relative to the corresponding value for the PPC) for the investigated grooved channels

$$\frac{Nu_m(\mathrm{BGC\ or\ GCV})/Nu(\mathrm{PPC})}{f(\mathrm{BGC\ or\ GCV})/f(\mathrm{PPC})} \tag{11}$$

to provide insight into the overall performance of the BGC and the GCV. In Fig. 10, the ratio described by Eq. (11) is displayed as function of the Reynolds number. The results suggest that the performance of the

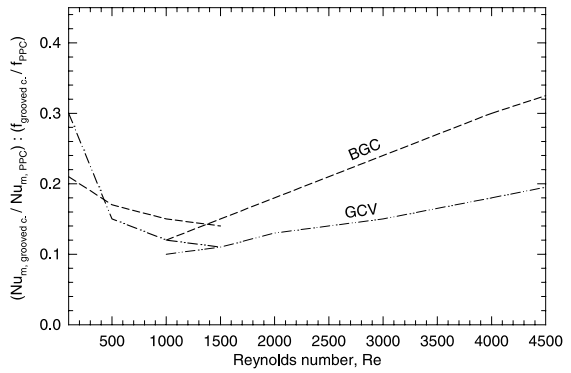

Fig. 10. Ratio of the measured channel-average Nusselt numbers Nu_m (relative to the corresponding value for the parallel plate channel) and the friction factor for the investigated grooved channels (again relative to the corresponding value for the PPC) as function od the Reynolds number Re.

GCV is superior in the low Reynolds number range, $Re < 500$. According to this comprehensive criterion, the BGC outperforms the GCV at higher Re, whereas the heat transfer performance alone of the GCV is always superior. Both performance curves exhibit a minimum in the region $600 < Re < 1600$. A performance evaluation and comparison of three channel geometries, the BGC, GCV and the same groove configuration equipped with cylinders in place of vanes, in terms of heat transfer (expressed through the Colburn factor) to pressure drop (expressed through the friction factor) ratio is discussed in a separate paper [12]. The analysis leads to similar conclusions for the BGC and the GCV.

6. Conclusions and outlook

The heat transfer enhancement technique considered in the paper, the strategic placement of curved vanes in the grooved channel, is suitable for improving the performance of single-phase convective cooling systems in situations where a moderate amount of enhancement is satisfactory. Heat transfer rates comparable to those in turbulent flow were achieved at lower Reynolds numbers; however, the associated pressure drop penalty is considerable. Heat transfer enhancement was mainly caused by the acceleration of the flow between the vane and the heated block and the elimination of the large recirculation region in the groove. Flow oscillations developing in the GCV contributed to heat transfer enhancement. Pressure drop data suggest that below a certain Reynolds number, for $Re < 1000$, the pressure drop penalty in the GCV is only moderately higher than for the BGC, therefore operating regimes in the lower Reynolds number range are favorable. Future experimental and computational studies focusing on optimizing the shape and placement of the vane are needed to devise solutions that reduce the pressure drop penalty.

Acknowledgements

This work is supported by the National Science Foundation Grants CTS-9310146 and CTS-9702943.

References

[1] C.H. Amon, B.B. Mikic, Numerical prediction of convective heat transfer in self-sustained oscillatory flows, J. Thermophys. Heat Transfer 4 (2) (1990) 239–246.
[2] C.H. Amon, D. Majumdar, C.V. Herman, F. Mayinger, B.B. Mikic, D.P. Sekulic, Numerical and experimental studies of self-sustained oscillatory flows in communicating channels, Int. J. Heat Mass Transfer 35 (1992) 3115–3129.
[3] A.M. Anderson, R.J. Moffat, Direct air cooling of electronic components: reducing component temperatures by controlled thermal mixing, J. Heat Transfer 113 (1991) 56–62.
[4] B. Farhanieh, C. Herman, B. Sunden, Numerical and experimental analysis of laminar fluid flow and forced convection heat transfer in a grooved duct, Int. J. Heat Mass Transfer 36 (6) (1993) 1609–1617.
[5] N.K. Ghaddar, K.Z. Korczak, B.B. Mikic, A.T. Patera, Numerical investigation of incompressible flow in grooved channels. Part 1. Stability and self-sustained oscillations, J. Fluid Mech. 163 (1986a) 99–127.
[6] N.K. Ghaddar, M. Magen, B.B. Mikic, A.T. Patera, Numerical investigation of incompressible flow in grooved channels. Part 2. Resonance and oscillatory heat transfer enhancement, J. Fluid Mech. 168 (1986b) 541–567.
[7] M. Greiner, An experimental investigation of resonant heat transfer enhancement in grooved channels, Int. J. Heat Mass Transfer 34 (6) (1991) 1383–1391.
[8] C.V. Herman, D. Mewes, F. Mayinger, Optical techniques in transport phenomena, in: A.S. Mujumdar, R.A. Mashelkar (Eds.), Advances in Transport Processes VIII, Elsevier, Amsterdam, 1992, pp. 1–58.
[9] C. Herman, E. Kang, M. Wetzel, Expanding the applications of holographic interferometry to the quantitative visualization of complex, oscillatory thermofluid processes, Exp. Fluids 24 (1998) 431–446.
[10] C. Herman, The impact of flow oscillations on convective heat transfer, in: C.-L. Tien (Ed.), Annual Review of Heat Transfer, vol. XI, 2000, pp. 495–562 (Chapter 8).
[11] C. Herman, E. Kang, Experimental visualization of temperature fields and study of heat transfer enhancement in oscillatory flow in a grooved channel, Heat Mass Transfer 37 (2001a) 87–99.
[12] C. Herman, E. Kang, Comparative evaluation of three heat transfer enhancement strategies in a grooved channel, Heat Mass Transfer 37 (2001b) 563–575.
[13] C. Herman, E. Kang, An experimental study of convective heat transfer enhancement in a grooved channel using cylindrical eddy promoters, J. Enhanced Heat Transfer 8 (2001) 1–19.

[14] O.C. Jones, An improvement in the calculation of turbulent friction factor in rectangular ducts, J. Fluids Eng. 2 (June) (1976) 173–181.
[15] J.S. Nigen, C. Amon, Forced convective cooling enhancement of electronic package configurations through self-sustained oscillatory flows, ASME J. Electron. Packaging 115 (1993) 356–365.
[16] R.M. Olson, Essentials of Engineering Fluid Mechanics, Harper & Row, New York, 1980.
[17] A.T. Patera, B.B. Mikic, Exploiting hydrodynamic instabilities. Resonant heat transfer enhancement, Int. J. Heat Mass Transfer 29 (8) (1986) 1127–1138.
[18] W. Rae, A. Pope, Low-Speed Wind Tunnel Testing, Wiley, New York, 1984.
[19] R.K. Shah, A.L. London, Laminar forced convection in ducts, in: T.F. Irvine, J.P. Hartnett (Eds.), Advances in Heat Transfer, Academic Press, New York, 1978, Suppl. 1.
[20] C.M. Vest, Holographic Interferometry, Wiley, New York, 1979.
[21] R.L. Webb, Principles of Enhanced Heat Transfer, Wiley, New York, 1994.
[22] F.M. White, Viscous Fluid Flow, McGraw-Hill, New York, 1991.